



High-throughput electronic band structure calculations: Challenges and tools

Wahyu Setyawan^a, Stefano Curtarolo^{a,b,*}

^a Dept. of Mechanical Engineering and Materials Science, Duke University, Durham, NC 27708, USA

^b Dept. of Physics, Duke University, Durham, NC 27708, USA

ARTICLE INFO

Article history:

Received 16 April 2010

Accepted 4 May 2010

Available online 15 June 2010

Keywords:

High-throughput
Combinatorial materials science
Computer simulation
Brillouin zone integration
VASP
AFLOW
ACONVASP

ABSTRACT

The article is devoted to the discussion of the high-throughput approach to band structures calculations. We present scientific and computational challenges as well as solutions relying on the developed framework (Automatic Flow, AFLOW/ACONVASP). The key factors of the method are the standardization and the robustness of the procedures. Two scenarios are relevant: (1) independent users generating databases in their own computational systems (off-line approach) and (2) teamed users sharing computational information based on a common ground (on-line approach). Both cases are integrated in the framework: for off-line approaches, the standardization is automatic and fully integrated for the 14 Bravais lattices, the primitive and conventional unit cells, and the coordinates of the high symmetry \mathbf{k} -path in the Brillouin zones. For on-line tasks, the framework offers an expandable web interface, where the user can prepare and set up calculations following the proposed standard. Few examples of band structures are included. LSDA+U parameters (U, J) are also presented for Nd, Sm, and Eu.

© 2010 Elsevier B.V. All rights reserved.

1. Introduction

Over the past decade computational materials science has undergone a tremendous growth thanks to the availability, power and relatively limited cost of high-performance computational equipment. The high-throughput (HT) method, started from the seminal paper by Xiang et al. for combinatorial discovery of superconductors [1], has become an effective and efficient tool for materials development [2–6] and prediction [7–13]. Recent examples of computational HT are the Pareto-optimal search for alloys and catalysts [14,15], the data-mining of quantum calculations method leading to the principle-component analysis of the formation energies of many alloys in several configurations [10–12,16,17], the high-throughput Kohn-anomalies search in ternary lithium-borides [18–20], and the multi-optimization techniques used for the study of high-temperature reactions in multicomponent hydrides [21–23].

In its practical implementation, HT uses some sort of automatic optimization technique to screen through a library of candidate compounds and to direct further refinements. The library can be a set of alloy prototypes [24,12] or a database of compounds such as the Pauling File [25] or the ICSD Database [26,27]. An important difference between the several-calculations and the HT philosophies is that the former concentrates on the calculation of a particular property, while the latter focuses on the extraction of property

correlations which are used to guide the search for systems with ad hoc characteristics. The power of HT comes with a cost. Due to the enormous amount of information produced, standardization and robustness of the procedures are necessary. This is especially true if one were concomitantly optimizing thermodynamics and electronic structure, which is required, for instance, in catalyst design [28], in accelerated “battery materials” discovery [29], and superconducting materials development [19,20]. Therefore a rational HT computational framework must contain a general, reliable, and standardized electronic structure analysis feature. It must determine the symmetry automatically, the Brillouin zone (BZ) integration path for all the possible 14 Bravais Lattices with all their various sub-cases, and put the direct and reciprocal lattice vectors in the appropriate standardized form, so that data can be exchanged and recycled between different projects. Although Brillouin zones integration paths have been included in books and literature for the last few decades [30–34], a standardized definition of the paths for all the different cases is, to the best of our knowledge, missing.

In this article, we describe the BZ paths features of AFLOW [35], which is our free framework for performing high-throughput thermodynamics and electronic structure calculations on top of DFT ab initio codes (currently the Vienna Ab-initio Simulation Package (VASP) but the porting to other DFT packages, such as Quantum Espresso [36] is underway). A typical task involves structural optimizations to a ground state (“relaxation run”), determination of charge density and its projection onto electronic orbitals (“static run”), and calculation of energy levels along a path of “important” wave vectors (“bands run”). We refer this set of \mathbf{k} -points as \mathbf{k} -path.

* Corresponding author at: Dept. of Mechanical Engineering and Materials Science, Duke University, Durham, NC 27708, USA.

E-mail address: stefano@duke.edu (S. Curtarolo).

Some definitions are pertinent for automatic construction of the \mathbf{k} -path. A \mathbf{k} -point is a *symmetry point* if its site symmetry contains at least one point symmetry operation that does not belong to the site symmetry of the neighboring points in sufficiently small vicinity. Similarly, a line or a plane forms a *symmetry line* or a *symmetry plane* if it contains at least one symmetry point and all of the \mathbf{k} -points on the line or plane have site symmetry with at least one point symmetry operation not possessed by the neighboring points. The \mathbf{k} -path must be carefully chosen so that the electronic properties of a materials imposed by its underlying crystal symmetry are correctly described. For example, GeF_4 (cl10, ICSD #202558, space group #217, I₄₃m) has an indirect gap. The conduction band minimum (CBM) occurs at point Γ , while the valence band maximum (VBM) occurs at the point H of the BZ for the body-centered cubic (BCC) lattice (Fig. 28). If a cubic unit cell were used instead the BCC, one would incorrectly find a direct gap occurring at point Γ .

The coordinates of symmetry \mathbf{k} -points are more conveniently expressed as fractions of the reciprocal lattice vectors. Therefore, the primitive lattice vectors needs to be properly defined in a standardized fashion. In order to build a primitive cell, the framework AFLOW performs the following procedure:

- i. Given any input structure (unit cell and the coordinates of the basis atoms), AFLOW reduces it into a minimal set of basis atoms in a primitive cell.
- ii. A set of symmetry properties are calculated: lattice point group, crystal point group, crystal family, factor group, space group operations, Pearson symbol, and the Bravais lattice type. If the input structure contains information about the space group number, it will be used to double check the Bravais lattice type.
- iii. A *standard conventional cell* is then identified and constructed, and whenever possible, the lattice vectors are ordered according to the axial lengths and the interaxial angles. This ordering eliminates some choices in the possible shapes of BZ in certain Bravais lattices. For example, let us consider the body-centered orthorhombic lattice. Depending on the ratios of the axial lengths the body-centered orthorhombic cell has three possible shapes of the BZ, and consequently three different coordinates of the symmetry points. By ordering the conventional lattice vectors so that $|\mathbf{a}_1| < |\mathbf{a}_2| < |\mathbf{a}_3|$ (i.e. $a < b < c$) a unique choice remains. Furthermore, the ordering improve the similarity between band structures of different compounds with the same lattice: the proportion between the length of each path segment in the band structure will be comparable.
- iv. From the ordered conventional unit cell, a *standard primitive cell* is created. Amongst all the possible primitive cells, AFLOW chooses the one with the reciprocal lattice vectors passing through the center of the Bragg planes belonging to the first BZ. The choice has considerable practical advantages. It enforces the reciprocal lattice vectors to be as perpendicular as possible within each other (Minkowski lattice reduction [37]) and minimizes the number of the plane waves basis set used in the quantum mechanical code, allowing faster convergence and smaller memory requirements.¹ After all these steps, the standard primitive unit cells of the 14 Bravais lattices as calculated by the AFLOW package are safe to be used in the “relaxation” and “static” calculations. As usual, the latter calculation will be used for the electronic density of states.

The \mathbf{k} -paths used in the band structure analysis are constructed from the irreducible part of the first Brillouin zone (IRBZ). A symmetry line is included in the path if it belongs to the edges of the IRBZ, otherwise it is included only if it carries one or more new point symmetry operations with respect to those of its extremes. Duplicate lines, due to the reciprocal lattice point group symmetry and translations are also omitted. A point possessing only identity (E) and inversion (I) operations cannot form a symmetry line, however, it may still be a zero-slope point [38]. Examples are point L in face-centered orthorhombic, points N , N_1 , and M in C-centered monoclinic, and all symmetry points in triclinic. To illustrate, TIF (oF8, ICSD #30268, space group #69, Fmmm) has CBM and VBM occurring at point L (Fig. 34). This result would have not been obtained if point L were excluded. Therefore, for completeness, a line from point Γ to such point is included in the \mathbf{k} -path.

Notably for triclinic, monoclinic, and rhombohedral systems, the shape of Wigner-Seitz cell of the reciprocal lattice depends nontrivially on the lattice vectors. For this reason, some researchers use the parallelepiped of primitive reciprocal lattice vectors, centered at $\mathbf{k} = \mathbf{0}$, to define a plausible BZ. Even though the energy is continuous throughout such BZ [30], its faces, in general, are not parallel to the symmetry planes of the lattice. Therefore, there is no guarantee that any line connecting two \mathbf{k} -points on a BZ face will be a symmetry line. In addition, since parallelepiped unit cells have only eight points, one at each corner of the IRBZ, one would miss some symmetry points on the Wigner-Seitz cell of reciprocal lattice. Consequently, a complete irreducible set of symmetry lines would not be obtained. For example if we were using a parallelepiped as BZ in the C-centered monoclinic variation MCLC₁ (Fig. 17), the site symmetries of points $\mathbf{b}_{1/2}$, $\mathbf{b}_{2/2}$, $(\mathbf{b}_1 + \mathbf{b}_3)/2$, and $(\mathbf{b}_2 + \mathbf{b}_3)/2$ would be only E and I . Therefore, the line $\mathbf{b}_{1/2} - \mathbf{Y}$ would not be, for example, a symmetry line. Furthermore, points like X , X_1 , I , and I_1 and their related symmetry lines (C_2 about x -axis) would not be included in such simplification. To conclude, although we believe that the simple parallelepiped BZ can be useful in some particular difficult cases, we think that the solution is not appropriate for a full automatic and high-throughput implementation of the band structure analysis. For this reason, inside the framework AFLOW, all the BZ and their \mathbf{k} -paths are derived from the Wigner-Seitz cell of the reciprocal lattice and the available symmetries. In Appendix A, for all the Bravais lattices and variations, we present the conventional and primitive lattice vectors implemented in AFLOW, the coordinates of high-symmetry \mathbf{k} -points for the path, the shape of the BZ, and an example of band structure calculation for a compound extracted from the ICSD database.

2. Off-line implementation

The effort in developing the standardized tool AFLOW comes from the ongoing generation of an extensive database of electronic band structure for inorganic crystals for scintillator materials design [39]. We have extracted approximately 195,000 structures from the Inorganic Crystal Structure Database (ICSD) [26,40,41,27]. AFLOW is equipped with utilities to select structures of interest. Selection criteria can be based on atomic number or element's name, mass density, number of atoms per primitive unit cell, chemical formula, structure prototype, space group number, lattice type, ICSD entry number, etc. Features to remove/include structures containing certain elements, partial occupancies, and redundancies (structures with the same chemical formula and space group number) are also implemented. Each structure is given a label which is composed of the structure's chemical formula (in alphabetic order) and the ICSD entry number. This label is the only information that AFLOW requires to produce the band structure. After the structure selection

¹ The common visualization softwares used for generating BZs simply take the input lattice vectors, generate reciprocal vectors and produce BZs which are not necessarily the Wigner-Seitz cells of the reciprocal lattice.

is performed, a list of labels is produced. Based on such labels, AFLOW creates a subdirectory for each structure and the necessary input file for the band structure calculation with VASP (porting to other DFT packages, such as Quantum Espresso [36] is underway). For running the DFT package, AFLOW has an option to run only one structure and exit, or to search through subfolders and run those that have not been calculated yet, or to wait for new structures to run. If started as a common Unix daemon through the queue of a computer cluster, AFLOW will generate, run, correct and converge many calculations per day, with minimum human input.

3. Electronic structure database implementation

The database of band structures under construction is calculated using VASP within the General Gradient Approximation of the density functional theory [42]. We use projector augmented waves pseudopotentials with exchange correlation functionals as parameterized by Perdew–Burke–Ernzerhof [43,44]. All structures are fully relaxed with a convergence tolerance of 1 meV/atom using dense grids of 3000–4000 \mathbf{k} -points per reciprocal atom for the integrations over BZ. A much denser grid of 10,000 is implemented for the static run to get accurate charge densities and density of states. Monkhorst–Pack scheme [45] is employed in the grid generation except for hexagonal and rhombohedral systems in which Γ -centered grid is selected for faster convergence. At the beginning of relaxation, a spin-polarized calculation is performed for all structures. Then, if the magnetization is smaller than $0.025\mu_B/\text{atom}$, the spin is turned off for the next relaxations and subsequent calculations to enhance the calculation speed. At the completion of each calculation (“relax” → “relax” → “static” → “bands”), appropriate MATLAB scripts are invoked for data analysis and visualization. All these steps are done automatically. One of the most difficult challenges in the high-throughput combinatorial search is about the response to erroneous interruption of the one or more of the flows working on a big set of problems, concurrently. The most common cause is insufficient hardware resources. Precaution must be taken, for example by estimating the memory requirement of the tasks, by grouping jobs based on memory, and by adapting the number of concurrent allocated CPUs with respect to the expected simulation speed. In addition, in many shared high-performance computer facilities, walltime is limited. This imposes a difficult problem because estimating computer time *a priori* is highly nontrivial, especially since the number of the required electronic and ionic relaxations depends on how distant the initial configuration is from the unknown final equilibrium. The second most common cause of interruption is due to runtime errors of VASP. AFLOW is capable of detecting most of the problems and it contains many self healing features. This is achieved by diagnosing the error message, self-correcting the appropriate parameters, and restarting VASP. With AFLOW, a job can be easily restarted from “relaxations”, “static”, or “bands” steps. AFLOW’s capability to continuously search and manage sub folders are not limited to DFT calculation. An “alien” mode is implemented, which allows AFLOW to execute other tasks in a high-throughput fashion. For instance, the many thousands Grand Canonical Monte Carlo calculations used in a recent surface science absorption project [46,47], were directed and performed by AFLOW. In addition, AFLOW is equipped with options to run a “pre” and “post” command/scripts that will be executed before and after the main program is performed in each folder, respectively. This allows AFLOW to generate input files on the fly depending on the results of different calculations, so that ad-hoc optimization can be implemented by the users. In conclusion, the “alien” mode and the “pre/post” command options improve the flexibility on the recovery from a crash or an unconverged run in a high-throughput manner as well as increase the overall versatility and throughput of AFLOW.

4. Implemented electronic properties

A typical information that one can extract from the band structure calculations includes the Fermi energy, band gap, type of the band gap, width of valence and conduction bands, effective mass of electron and hole, charge densities, band structures, total and partial density of states, etc. A user can easily create utilities in any language at choice for data analysis, and use AFLOW in “alien” mode to execute the utilities automatically in each subfolder. For our purpose we have chosen MATLAB, which has produced all the band structures and orbital-projected total density of states for every shape the BZ as presented in Appendix A.

5. LSDA+U corrections

It is generally known that due to a rather weak orbital-dependence of the DFT’s exchange correlation energy, the strong on-site Coulomb repulsion in systems with narrow d- and f-bands is underaccounted. As a result, DFT produces bandgaps that are smaller than experimental values and some times it fails to get the correct ground state in such systems. Based on our experience in calculating the electronic structure of many lanthanum halides, DFT incorrectly gives conduction band minima with 4f states instead of 5d orbitals. The insufficient description of strongly correlated systems given by DFT, can be remedied, at least partially, by GW [48] or LSDA+U corrections. Due to their large computational cost, GW corrections are not currently applicable for high-throughput searches. When needed, LSDA+U corrections are automatically implemented by AFLOW, based on the formulas developed by Duradev [49] and Liechtenstein [50]. To the best of our knowledge, there are no systematic studies for the Hubbard U and the screened Stoner exchange parameters J across all the elements with all the possible oxidation states. Detailed analysis and determination of the U and J values for different compounds would be one of the tasks of high-throughput future research [51]. In the mean time, we have applied the + U corrections to the 4f-wave functions of lanthanide compounds to get the correct orbitals at the conduction band minimum. For the systems not available in literature but related to our current research, Nd, Sm, and Eu, we have fit U and J so that the 4f levels reproduce the experimental density of states from the X-ray photoelectron spectroscopy and Bremsstrahlung isochromat spectroscopy (XPS-BIS) measurements [52]. Although the data is for metals, we are confident that the values of U and J for other compounds will not be very different from the fit. The values are listed in Table 1.

6. On-line implementation: ACONVASP-online

Users who do not need to perform high-throughput calculations or to create databases, can prepare standard unit cells input files and extract the appropriate \mathbf{k} -points path by using the command version of AFLOW called ACONVASP or the on-line tool ACONVASP-online available in our website (<http://materials.duke.edu>).

Table 1

Default value of U and J parameters given in eV applied to f-orbitals within the GGA+U approximation included in AFLOW. Note that these parameters are subject to update.

Atom	U	J	Ref.	Atom	U	J	Ref.
La	8.1	0.6	[53]	Eu	6.4	1.0	
Ce	7.0	0.7	[54]	Gd	6.7	0.7	[55]
Pr	6.5	1.0	[56]	Tm	7.0	1.0	[57]
Nd	7.2	1.0		Yb	7.0	0.67	[58]
Sm	7.4	1.0		Lu	4.8	0.95	[53]

The following protocol should be followed. Unit cells must first be reduced to standard primitives, then they should be appropriately relaxed (if needed). Before the static run, the cells should be reduced again to standard primitive (symmetry and orientation might have changed during the relaxation). The user should then perform the static run and then project the eigenvalues along the directions which are specified in the “kpath” option. If the user is running AFLOW and VASP, the web interface can also prepare a template input file “aflow.in” which performs all the mentioned tasks.

Acknowledgments

We thank Romain Gaume, Stephanie Lam, Robert Feigelson, Ohad Levy, Mike Mehl, Gus Hart, Leeor Kronik, Roman Chepulskyy and Michal Jahnátek for fruitful discussions. Research supported by ONR (N00014-07-1-0878, N00014-07-1-1085, N00014-09-1-0921, and N00014-10-1-0436), and NSF (DMR-0639822 and DMR-0650406). We are grateful for extensive use of the Teragrid resources (MCA-07S005). SC acknowledges the Feinberg support at the Weizmann Institute of Science.

Appendix A

The choice of lattice vectors implemented in AFLOW is given here. When the primitive lattice is the same as the conventional one, it is simply called “lattice”. Variables a , b , c , α , β , γ denote the axial lengths and interaxial angles of the conventional lattice vectors, while k_a , k_b , k_c , k_α , k_β , k_γ are those of the primitive reciprocal lattice vectors \mathbf{b}_1 , \mathbf{b}_2 , \mathbf{b}_3 . The coordinates of symmetry \mathbf{k} -points are given in fractions of \mathbf{b}_1 , \mathbf{b}_2 , \mathbf{b}_3 .

A.1. Cubic (CUB, cP)

Lattice (see Fig. 1 and Table 2)

$$\begin{aligned}\mathbf{a}_1 &= (a, 0, 0) \\ \mathbf{a}_2 &= (0, a, 0) \\ \mathbf{a}_3 &= (0, 0, a)\end{aligned}$$

A.2. Face-centered cubic (FCC, cF)

(See Fig. 2 and Table 3.)

Conventional lattice

$$\begin{aligned}\mathbf{a}_1 &= (a, 0, 0) \\ \mathbf{a}_2 &= (0, a, 0) \\ \mathbf{a}_3 &= (0, 0, a)\end{aligned}$$

Primitive lattice

$$\begin{aligned}\mathbf{a}_1 &= (0, a/2, a/2) \\ \mathbf{a}_2 &= (a/2, 0, a/2) \\ \mathbf{a}_3 &= (a/2, a/2, 0)\end{aligned}$$

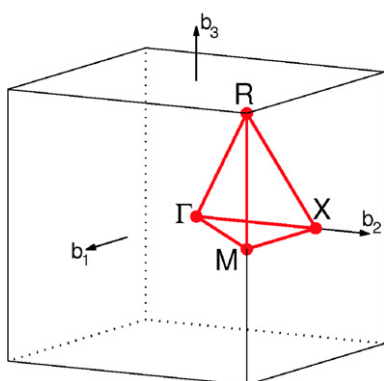


Fig. 1. Brillouin zone of CUB lattice. Path: $\Gamma-X-M-\Gamma-R-X|M-R$. An example of band structure using this path is given in Fig. 26.

Table 2
Symmetry \mathbf{k} -points of CUB lattice.

$\times \mathbf{b}_1$	$\times \mathbf{b}_2$	$\times \mathbf{b}_3$		$\times \mathbf{b}_1$	$\times \mathbf{b}_2$	$\times \mathbf{b}_3$	
0	0	0	Γ	1/2	1/2	1/2	R
1/2	1/2	0	M	0	1/2	0	X

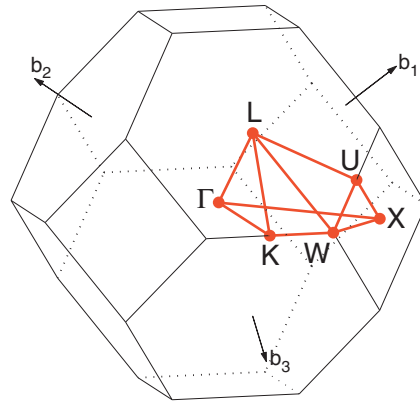


Fig. 2. Brillouin zone of FCC lattice. Path: $\Gamma-X-W-K-\Gamma-L-U-W-L-K|U-X$. An example of band structure using this path is given in Fig. 27.

Table 3
Symmetry \mathbf{k} -points of FCC lattice.

$\times \mathbf{b}_1$	$\times \mathbf{b}_2$	$\times \mathbf{b}_3$		$\times \mathbf{b}_1$	$\times \mathbf{b}_2$	$\times \mathbf{b}_3$	
0	0	0	Γ	5/8	1/4	5/8	U
3/8	3/8	3/4	K	1/2	1/4	3/4	W
1/2	1/2	1/2	L	1/2	0	1/2	X

A.3. Body-centered cubic (BCC, cl)

(See Fig. 3 and Table 4.)

Conventional lattice

$$\begin{aligned}\mathbf{a}_1 &= (a, 0, 0) \\ \mathbf{a}_2 &= (0, a, 0) \\ \mathbf{a}_3 &= (0, 0, a)\end{aligned}$$

Primitive lattice

$$\begin{aligned}\mathbf{a}_1 &= (-a/2, a/2, a/2) \\ \mathbf{a}_2 &= (a/2, -a/2, a/2) \\ \mathbf{a}_3 &= (a/2, a/2, -a/2)\end{aligned}$$

A.4. Tetragonal (TET, tP)

Lattice (see Fig. 4 and Table 5)

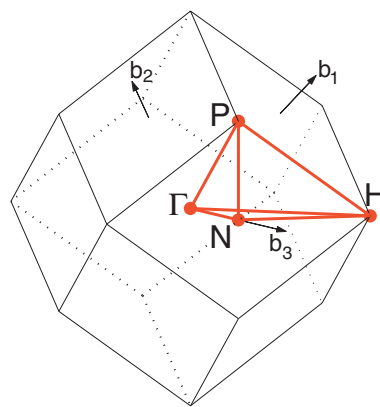
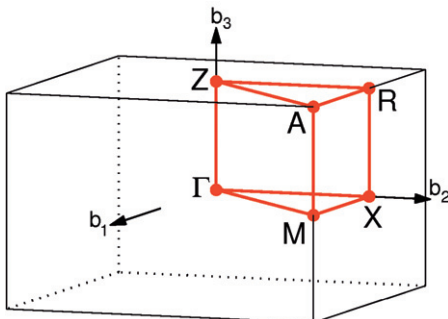


Fig. 3. Brillouin zone of BCC lattice. Path: $\Gamma-H-N-\Gamma-P-H|P-N$. An example of band structure using this path is given in Fig. 28.

Table 4

Symmetry k-points of BCC lattice.

$\times \mathbf{b}_1$	$\times \mathbf{b}_2$	$\times \mathbf{b}_3$	$\times \mathbf{b}_1$	$\times \mathbf{b}_2$	$\times \mathbf{b}_3$
0	0	0	Γ	1/4	1/4
1/2	-1/2	1/2	H	0	0

**Fig. 4.** Brillouin zone of TET lattice. Path: $\Gamma-X-M-\Gamma-Z-R-A-Z|X-R|M-A$. An example of band structure using this path is given in Fig. 29.**Table 5**

Symmetry k-points of TET lattice.

$\times \mathbf{b}_1$	$\times \mathbf{b}_2$	$\times \mathbf{b}_3$	$\times \mathbf{b}_1$	$\times \mathbf{b}_2$	$\times \mathbf{b}_3$
0	0	0	Γ	0	1/2
1/2	1/2	1/2	A	0	1/2
1/2	1/2	0	M	0	0

$$\begin{aligned}\mathbf{a}_1 &= (a, 0, 0) \\ \mathbf{a}_2 &= (0, a, 0) \\ \mathbf{a}_3 &= (0, 0, c)\end{aligned}$$

A.5. Body-centered tetragonal (BCT, tI)

(See Figs. 5 and 6 and Tables 6 and 7.)

Conventional lattice

$$\begin{aligned}\mathbf{a}_1 &= (a, 0, 0) \\ \mathbf{a}_2 &= (0, a, 0) \\ \mathbf{a}_3 &= (0, 0, c)\end{aligned}$$

Primitive lattice

$$\begin{aligned}\mathbf{a}_1 &= (-a/2, a/2, c/2) \\ \mathbf{a}_2 &= (a/2, -a/2, c/2) \\ \mathbf{a}_3 &= (a/2, a/2, -c/2)\end{aligned}$$

Variations:

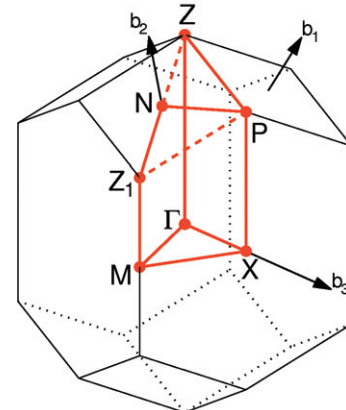
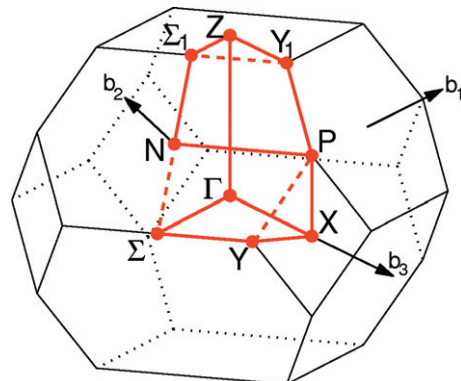
BCT₁ : $c < a$ BCT₂ : $c > a$

A.6. Orthorhombic (ORC, oP)

Ordering of the conventional lattice: $a < b < c$. Lattice (see Fig. 7 and Table 8)

$$\begin{aligned}\mathbf{a}_1 &= (a, 0, 0) \\ \mathbf{a}_2 &= (0, b, 0) \\ \mathbf{a}_3 &= (0, 0, c)\end{aligned}$$

A.7. Face-centered orthorhombic (ORCF, oF)

Ordering of the conventional lattice: $a < b < c$. (See Figs. 8–10 and Tables 9 and 10.)**Fig. 5.** Brillouin zone of BCT₁ lattice. Path: $\Gamma-X-M-\Gamma-Z-P-N-Z_1-M|X-P$. An example of band structure using this path is given in Fig. 30.**Fig. 6.** Brillouin zone of BCT₂ lattice. Path: $\Gamma-X-Y-\Sigma-\Gamma-Z-\Sigma_1-N-P-Y_1-Z|X-P$. An example of band structure using this path is given in Fig. 31.**Table 6**Symmetry k-points of BCT₁ lattice.

$\times \mathbf{b}_1$	$\times \mathbf{b}_2$	$\times \mathbf{b}_3$	$\times \mathbf{b}_1$	$\times \mathbf{b}_2$	$\times \mathbf{b}_3$
0	0	0	Γ	0	0
-1/2	1/2	1/2	M	η	η
0	1/2	0	N	- η	$1-\eta$
1/4	1/4	1/4	P		η
$\eta = (1 + c^2/a^2)/4$					Z_1

Table 7Symmetry k-points of BCT₂ lattice.

$\times \mathbf{b}_1$	$\times \mathbf{b}_2$	$\times \mathbf{b}_3$	$\times \mathbf{b}_1$	$\times \mathbf{b}_2$	$\times \mathbf{b}_3$
0	0	0	Γ	0	0
0	1/2	0	N	$-\zeta$	ζ
1/4	1/4	1/4	P	1/2	1/2
$-\eta$	η	η	Σ	1/2	$-\zeta$
η	$1-\eta$	$-\eta$	Σ_1	1/2	$-1/2$
$\eta = (1 + a^2/c^2)/4$					Z
					$\zeta = a^2/(2c^2)$

Conventional lattice

$$\begin{aligned}\mathbf{a}_1 &= (a, 0, 0) \\ \mathbf{a}_2 &= (0, b, 0) \\ \mathbf{a}_3 &= (0, 0, c)\end{aligned}$$

Primitive lattice

$$\begin{aligned}\mathbf{a}_1 &= (0, b/2, c/2) \\ \mathbf{a}_2 &= (a/2, 0, c/2) \\ \mathbf{a}_3 &= (a/2, b/2, 0)\end{aligned}$$

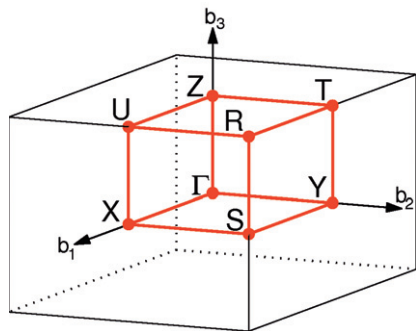


Fig. 7. Brillouin zone of ORC lattice. Path: $\Gamma-X-S-Y-\Gamma-Z-U-R-T-Z|Y-T|U-X|S-R$. An example of band structure using this path is given in Fig. 32.

Table 8

Symmetry \mathbf{k} -points of ORC.

$\times \mathbf{b}_1$	$\times \mathbf{b}_2$	$\times \mathbf{b}_3$	$\times \mathbf{b}_1$	$\times \mathbf{b}_2$	$\times \mathbf{b}_3$	
0	0	0	Γ	1/2	0	1/2
1/2	1/2	1/2	R	1/2	0	X
1/2	1/2	0	S	0	1/2	Y
0	1/2	1/2	T	0	0	Z

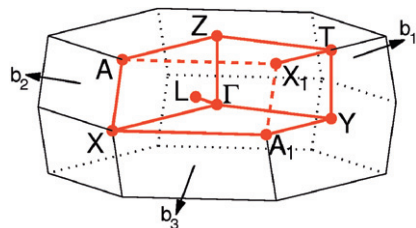


Fig. 8. Brillouin zone of ORCF₁ lattice. Path: $\Gamma-Y-T-Z-\Gamma-X-A_1-Y|T-X_1|X-A-Z|L-\Gamma$. An example of band structure using this path is given in Fig. 33.

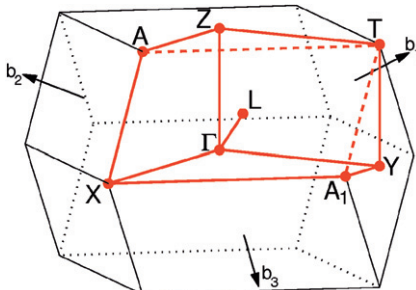


Fig. 9. Brillouin zone of ORCF₃ lattice. Path: $\Gamma-Y-T-Z-\Gamma-X-A_1-Y|X-A-Z|L-\Gamma$. An example of band structure using this path is given in Fig. 35.

Variations:

$$\text{ORCF}_1 : 1/a^2 > 1/b^2 + 1/c^2$$

$$\text{ORCF}_2 : 1/a^2 < 1/b^2 + 1/c^2$$

$$\text{ORCF}_3 : 1/a^2 = 1/b^2 + 1/c^2$$

A.8. Body-centered orthorhombic (ORCI, oI)

Ordering of the conventional lattice: $a < b < c$. (See Fig. 11 and Table 11.)

Conventional lattice

$$\mathbf{a}_1 = (a, 0, 0)$$

$$\mathbf{a}_2 = (0, b, 0)$$

$$\mathbf{a}_3 = (0, 0, c)$$

Primitive lattice

$$\mathbf{a}_1 = (-a/2, b/2, c/2)$$

$$\mathbf{a}_2 = (a/2, -b/2, c/2)$$

$$\mathbf{a}_3 = (a/2, b/2, -c/2)$$

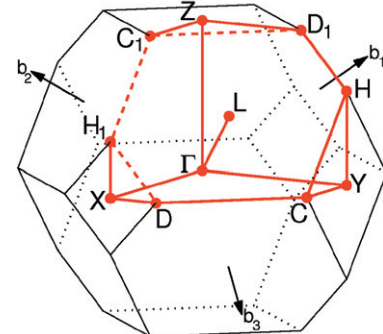


Fig. 10. Brillouin zone of ORCF₂ lattice. Path: $\Gamma-Y-C-D-X-\Gamma-Z-D_1-H-C|C_1-Z|X-H_1|H-Y|L-\Gamma$. An example of band structure using this path is given in Fig. 34.

Table 9

Symmetry \mathbf{k} -points of ORCF₁ and ORCF₃.

$\times \mathbf{b}_1$	$\times \mathbf{b}_2$	$\times \mathbf{b}_3$	$\times \mathbf{b}_1$	$\times \mathbf{b}_2$	$\times \mathbf{b}_3$
0	0	0	Γ	0	η
1/2	$1/2 + \zeta$	ζ	A	1	$1 - \eta$
1/2	$1/2 - \zeta$	$1 - \zeta$	A_1	$1/2$	$1/2$
1/2	$1/2$	$1/2$	L	$1/2$	0
1	$1/2$	$1/2$	T	$1/2$	$1/2$

$\zeta = (1 + a^2/b^2 - a^2/c^2)/4$, $\eta = (1 + a^2/b^2 + a^2/c^2)/4$

Table 10

Symmetry \mathbf{k} -points of ORCF₂.

$\times \mathbf{b}_1$	$\times \mathbf{b}_2$	$\times \mathbf{b}_3$	$\times \mathbf{b}_1$	$\times \mathbf{b}_2$	$\times \mathbf{b}_3$
0	0	0	Γ	$1 - \phi$	$1/2 - \phi$
1/2	$1/2 - \eta$	$1 - \eta$	C	ϕ	$1/2 + \phi$
1/2	$1/2 + \eta$	η	C_1	0	$1/2$
$1/2 - \delta$	$1/2$	$1 - \delta$	D	$1/2$	0
$1/2 + \delta$	$1/2$	δ	D_1	$1/2$	$1/2$
1/2	$1/2$	$1/2$	L	$1/2$	0

$\eta = (1 + a^2/b^2 - a^2/c^2)/4$, $\delta = (1 + b^2/a^2 - b^2/c^2)/4$, $\phi = (1 + c^2/b^2 - c^2/a^2)/4$

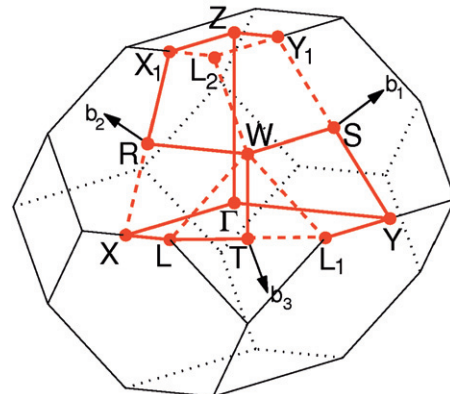


Fig. 11. Brillouin zone of ORCI lattice. Path: $\Gamma-X-L-T-W-R-X_1-Z-\Gamma-Y-S-W|L_1-Y_1-Z$. An example of band structure using this path is given in Fig. 36.

A.9. C-centered orthorhombic (ORCC, oS)

Ordering of the conventional lattice: $a < b$. (See Fig. 12 and Table 12.)

Table 11
Symmetry \mathbf{k} -points of ORCI.

$\times \mathbf{b}_1$	$\times \mathbf{b}_2$	$\times \mathbf{b}_3$	$\times \mathbf{b}_1$	$\times \mathbf{b}_2$	$\times \mathbf{b}_3$
0	0	0	Γ	$1/4$	$1/4$
$-\mu$	μ	$1/2 - \delta$	L	$-\zeta$	ζ
μ	$-\mu$	$1/2 + \delta$	L_1	ζ	$1 - \zeta$
$1/2 - \delta$	$1/2 + \delta$	$-\mu$	L_2	η	$-\eta$
0	$1/2$	0	R	$1 - \eta$	η
$1/2$	0	0	S	$1/2$	$-1/2$
0	0	$1/2$	T		
$\zeta = (1 + a^2/c^2)/4$,			$\delta = (b^2 - a^2)/(4c^2)$		
$\eta = (1 + b^2/c^2)/4$,			$\mu = (a^2 + b^2)/(4c^2)$		

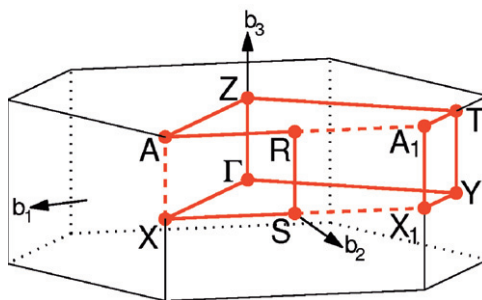


Fig. 12. Brillouin zone of ORCC lattice. Path: $\Gamma-X-S-R-A-Z-\Gamma-Y-X_1-A_1-T-Y|Z-T$. An example of band structure using this path is given in Fig. 37.

Table 12
Symmetry \mathbf{k} -points of ORCC.

$\times \mathbf{b}_1$	$\times \mathbf{b}_2$	$\times \mathbf{b}_3$	$\times \mathbf{b}_1$	$\times \mathbf{b}_2$	$\times \mathbf{b}_3$
0	0	0	Γ	$-1/2$	$1/2$
ζ	ζ	$1/2$	A	ζ	0
$-\zeta$	$1 - \zeta$	$1/2$	A_1	$-\zeta$	$1 - \zeta$
0	$1/2$	$1/2$	R	$-1/2$	$1/2$
0	$1/2$	0	S	0	$1/2$
$\zeta = (1 + a^2/b^2)/4$					

Conventional lattice
 $\mathbf{a}_1 = (a, 0, 0)$
 $\mathbf{a}_2 = (0, b, 0)$
 $\mathbf{a}_3 = (0, 0, c)$

Primitive lattice
 $\mathbf{a}_1 = (a/2, -b/2, 0)$
 $\mathbf{a}_2 = (a/2, b/2, 0)$
 $\mathbf{a}_3 = (0, 0, c)$

A.10. Hexagonal (HEX, hP)

Lattice (see Fig. 13 and Table 13)

$$\begin{aligned}\mathbf{a}_1 &= \left(a/2, -\left(a\sqrt{3}\right)/2, 0\right) \\ \mathbf{a}_2 &= \left(a/2, \left(a\sqrt{3}\right)/2, 0\right) \\ \mathbf{a}_3 &= (0, 0, c)\end{aligned}$$

A.11. Rhombohedral (RHL, hR)

Lattice (see Figs. 14 and 15 and Tables 14 and 15)

$$\begin{aligned}\mathbf{a}_1 &= (a \cos(\alpha/2), -a \sin(\alpha/2), 0) \\ \mathbf{a}_2 &= (a \cos(\alpha/2), a \sin(\alpha/2), 0) \\ \mathbf{a}_3 &= (a \cos \alpha / \cos(\alpha/2), 0, a \sqrt{1 - \cos^2 \alpha / \cos^2(\alpha/2)})\end{aligned}$$

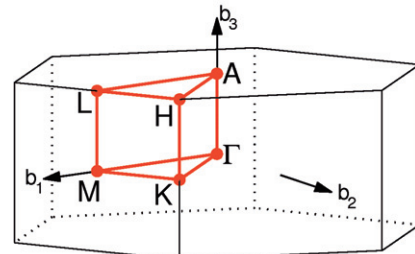


Fig. 13. Brillouin zone of HEX lattice. Path: $\Gamma-M-K-\Gamma-A-L-H-A|\Gamma-L-M|K-H$. An example of band structure using this path is given in Fig. 38.

Table 13
Symmetry \mathbf{k} -points of HEX.

$\times \mathbf{b}_1$	$\times \mathbf{b}_2$	$\times \mathbf{b}_3$	$\times \mathbf{b}_1$	$\times \mathbf{b}_2$	$\times \mathbf{b}_3$
0	0	0	Γ	$1/3$	$1/3$
0	0	$1/2$	A	$1/2$	0
$1/3$	$1/3$	$1/2$	H	$1/2$	0

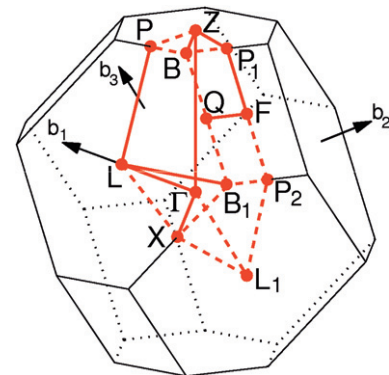


Fig. 14. Brillouin zone of RHL₁ lattice. Path: $\Gamma-L-B_1|B-Z-\Gamma-X|Q-F-P_1-Z|L-P$. An example of band structure using this path is given in Fig. 39.

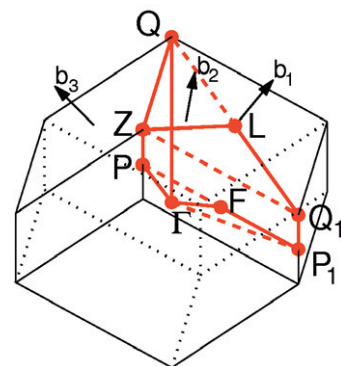


Fig. 15. Brillouin zone of RHL₂ lattice. Path: $\Gamma-P-Z-Q-\Gamma-F-P_1-Q_1-L-Z$. An example of band structure using this path is given in Fig. 40.

Variations:

RHL₁ : $\alpha < 90^\circ$

RHL₂ : $\alpha > 90^\circ$

A.12. Monoclinic (MCL, mP)

Ordering of the lattice: $a, b \leq c, \alpha < 90^\circ, \beta = \gamma = 90^\circ$.

Table 14Symmetry k-points of RHL₁.

$\times \mathbf{b}_1$	$\times \mathbf{b}_2$	$\times \mathbf{b}_3$	$\times \mathbf{b}_1$	$\times \mathbf{b}_2$	$\times \mathbf{b}_3$
0	0	0	Γ	η	v
η	$1/2$	$1-\eta$	B	$1-v$	$1-\eta$
$1/2$	$1-\eta$	$\eta-1$	B_1	v	$\eta-1$
$1/2$	$1/2$	0	F	$1-v$	v
$1/2$	0	0	L	v	0
0	0	$-1/2$	L_1	$1/2$	$1/2$
$\eta = (1 + 4 \cos \alpha)/(2 + 4 \cos \alpha)$					
$v = 3/4 - \eta/2$					

Table 15Symmetry k-points of RHL₂.

$\times \mathbf{b}_1$	$\times \mathbf{b}_2$	$\times \mathbf{b}_3$	$\times \mathbf{b}_1$	$\times \mathbf{b}_2$	$\times \mathbf{b}_3$
0	0	0	Γ	v	$v-1$
$1/2$	$-1/2$	0	F	η	η
$1/2$	0	0	L	$1-\eta$	$-\eta$
$1-v$	$-v$	$1-v$	P	$1/2$	$-1/2$
$\eta = 1/(2 \tan^2(\alpha/2))$					
$v = 3/4 - \eta/2$					

Lattice (see Fig. 16 and Table 16)

$$\mathbf{a}_1 = (a, 0, 0)$$

$$\mathbf{a}_2 = (0, b, 0)$$

$$\mathbf{a}_3 = (0, c \cos \alpha, c \sin \alpha)$$

A.13. C-centered monoclinic (MCLC, mS)

Ordering of the conventional lattice: $a, b \leq c, \alpha < 90^\circ, \beta = \gamma = 90^\circ$. (Figs. 17–21 and Tables 17–19).

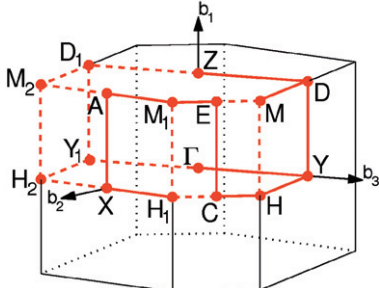


Fig. 16. Brillouin zone of MCL lattice. Path: $\Gamma-Y-H-C-E-M_1-A-X-H_1|M-D-Z|Y-D$. An example of band structure using this path is given in Fig. 41.

Table 16

Symmetry k-points of MCL.

$\times \mathbf{b}_1$	$\times \mathbf{b}_2$	$\times \mathbf{b}_3$	$\times \mathbf{b}_1$	$\times \mathbf{b}_2$	$\times \mathbf{b}_3$
0	0	0	Γ	0	η
$1/2$	$1/2$	0	A	$1/2$	η
0	$1/2$	$1/2$	C	$1/2$	$1-\eta$
$1/2$	0	$1/2$	D	$1/2$	η
$1/2$	0	$-1/2$	D_1	0	$1/2$
$1/2$	$1/2$	$1/2$	E	0	0
0	η	$1-v$	H	0	$1/2$
0	$1-\eta$	v	H_1	$1/2$	0
$\eta = (1 - b \cos \alpha/c)/(2 \sin^2 \alpha)$					
$v = 1/2 - \eta c \cos \alpha/b$					

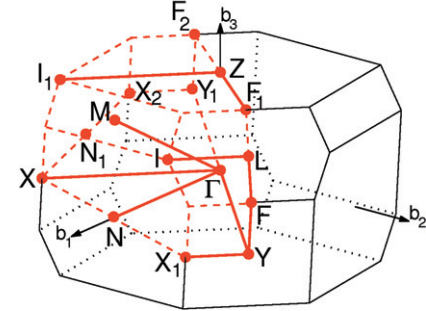


Fig. 17. Brillouin zone of MCLC₁ lattice. Path: $\Gamma-Y-F-L-I|I_1-Z-F_1|Y-X_1|X-\Gamma-N|M-\Gamma$. An example of band structure using this path is given in Fig. 42.

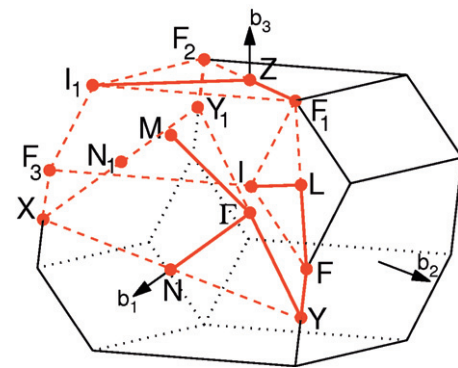


Fig. 18. Brillouin zone of MCLC₂ lattice. Note that Y is equivalent to X. Path: $\Gamma-Y-F-L-I|I_1-Z-F_1|N-\Gamma-M$. An example of band structure using this path is given in Fig. 43.

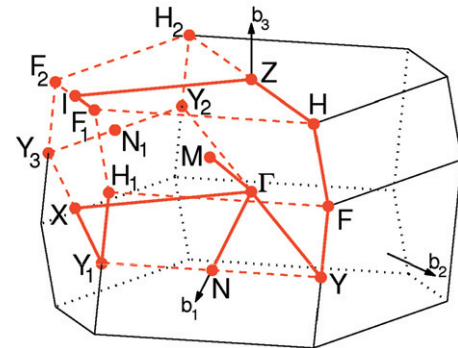


Fig. 19. Brillouin zone of MCLC₃ lattice. Path: $\Gamma-Y-F-H-Z-I-F_1|H_1-Y_1-X_1|X-\Gamma-N|M-\Gamma$. An example of band structure using this path is given in Fig. 44.

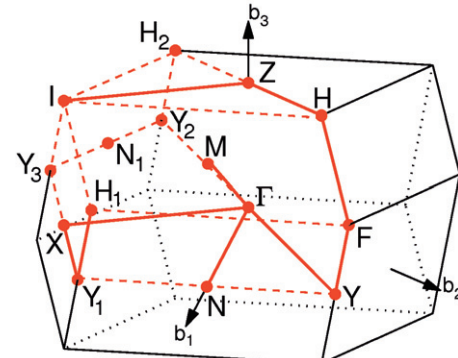


Fig. 20. Brillouin zone of MCLC₄ lattice. Note that I is equivalent to F. Path: $\Gamma-Y-F-H-Z-I|H_1-Y_1-X_1|X-\Gamma-N|M-\Gamma$. An example of band structure using this path is given in Fig. 45.

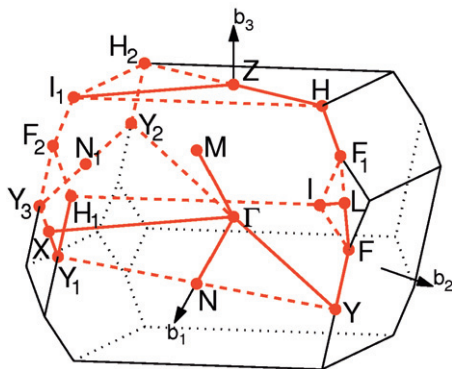


Fig. 21. Brillouin zone of MCLC₅ lattice. Path: $\Gamma-Y-F-L-I|I_1-Z-H-F_1|H_1-Y_1-X-\Gamma-N|M-\Gamma$. An example of band structure using this path is given in Fig. 46.

Table 17
Symmetry \mathbf{k} -points of MCLC₁ and MCLC₂.

$\times \mathbf{b}_1$	$\times \mathbf{b}_2$	$\times \mathbf{b}_3$	$\times \mathbf{b}_1$	$\times \mathbf{b}_2$	$\times \mathbf{b}_3$	
0	0	0	Γ	1/2	1/2	L
1/2	0	0	N	1/2	0	M
0	-1/2	0	N_1	1 - ψ	ψ - 1	X
1 - ζ	1 - ζ	1 - η	F	ψ	1 - ψ	X_1
ζ	ζ	η	F_1	ψ - 1	- ψ	X_2
- ζ	- ζ	1 - η	F_2	1/2	1/2	Y
1 - ζ	- ζ	1 - η	F_3	-1/2	-1/2	Y_1
ϕ	1 - ϕ	1/2	I	0	0	Z
1 - ϕ	ϕ - 1	1/2	I_1			
$\zeta = (2 - b \cos \alpha/c)/(4 \sin^2 \alpha)$						
$\eta = 1/2 + 2\zeta c \cos \alpha/b$						
$\psi = 3/4 - a^2/(4b^2 \sin^2 \alpha)$						
$\phi = \psi + (3/4 - \psi)b \cos \alpha/c$						

Table 18
Symmetry \mathbf{k} -points of MCLC₃ and MCLC₄.

$\times \mathbf{b}_1$	$\times \mathbf{b}_2$	$\times \mathbf{b}_3$	$\times \mathbf{b}_1$	$\times \mathbf{b}_2$	$\times \mathbf{b}_3$	
0	0	0	Γ	1/2	0	N
1 - ϕ	1 - ϕ	1 - ψ	F	0	-1/2	N_1
ϕ	ϕ - 1	ψ	F_1	1/2	-1/2	X
1 - ϕ	- ϕ	1 - ψ	F_2	μ	μ	Y
ζ	ζ	η	H	1 - μ	- μ	Y_1
1 - ζ	- ζ	1 - η	H_1	- μ	- μ	Y_2
- ζ	- ζ	1 - η	H_2	μ	μ - 1	Y_3
1/2	-1/2	1/2	I	0	0	Z
1/2	0	1/2	M			
$\mu = (1 + b^2/a^2)/4$						
$\delta = bc \cos \alpha/(2a^2)$						
$\zeta = \mu - 1/4 + (1 - b \cos \alpha/c)/(4 \sin^2 \alpha)$						
$\eta = 1/2 + 2\zeta c \cos \alpha/b$						
$\phi = 1 + \zeta - 2\mu$						
$\psi = \eta - 2\delta$						

Conventional lattice

$$\begin{aligned}\mathbf{a}_1 &= (a, 0, 0) \\ \mathbf{a}_2 &= (0, b, 0) \\ \mathbf{a}_3 &= (0, c \cos \alpha, c \sin \alpha)\end{aligned}$$

Variations:

- MCLC₁ : $k_y > 90^\circ$
- MCLC₂ : $k_y = 90^\circ$
- MCLC₃ : $k_y < 90^\circ$, $b \cos \alpha/c + b^2 \sin^2 \alpha/a^2 < 1$
- MCLC₄ : $k_y < 90^\circ$, $b \cos \alpha/c + b^2 \sin^2 \alpha/a^2 = 1$
- MCLC₅ : $k_y < 90^\circ$, $b \cos \alpha/c + b^2 \sin^2 \alpha/a^2 > 1$

Primitive lattice

$$\begin{aligned}\mathbf{a}_1 &= (a/2, b/2, 0) \\ \mathbf{a}_2 &= (-a/2, b/2, 0) \\ \mathbf{a}_3 &= (0, c \cos \alpha, c \sin \alpha)\end{aligned}$$

Table 19
Symmetry \mathbf{k} -points of MCLC₅.

$\times \mathbf{b}_1$	$\times \mathbf{b}_2$	$\times \mathbf{b}_3$	$\times \mathbf{b}_1$	$\times \mathbf{b}_2$	$\times \mathbf{b}_3$	
0	0	0	Γ	1/2	0	M
v	v	ω	F	1/2	0	N
$1 - v$	$1 - v$	$1 - \omega$	F_1	0	-1/2	N_1
v	$v - 1$	ω	F_2	1/2	-1/2	X
ζ	ζ	η	H	μ	μ	Y
$1 - \zeta$	- ζ	$1 - \eta$	H_1	$1 - \mu$	- μ	Y_1
- ζ	- ζ	$1 - \eta$	H_2	- μ	- μ	Y_2
ρ	$1 - \rho$	1/2	I	μ	μ - 1	Y_3
$1 - \rho$	$\rho - 1$	1/2	I_1	0	0	Z
1/2	1/2	1/2	L			
$\zeta = (b^2/a^2 + (1 - b \cos \alpha/c)/\sin^2 \alpha)/4$						
$\mu = \eta/2 + b^2/(4a^2) - bc \cos \alpha/(2a^2)$						
$\omega = (4v - 1 - b^2 \sin^2 \alpha/a^2)c/(2b \cos \alpha)$						
$\eta = 1/2 + 2\zeta c \cos \alpha/b$						
$\delta = \zeta c \cos \alpha/b + \omega/2 - 1/4$						
$\rho = 1 - \zeta a^2/b^2$						

A.14. Triclinic (TRI, aP)

Lattice (see Figs. 22–25 and Tables 20 and 21)

$$\mathbf{a}_1 = (a, 0, 0)$$

$$\mathbf{a}_2 = (b \cos \gamma, b \sin \gamma, 0)$$

$$\mathbf{a}_3 = \left(c \cos \beta, \frac{c}{\sin \gamma} [\cos \alpha - \cos \beta \cos \gamma], \frac{c}{\sin \gamma} \sqrt{\sin^2 \gamma - \cos^2 \alpha - \cos^2 \beta + 2 \cos \alpha \cos \beta \cos \gamma} \right)$$

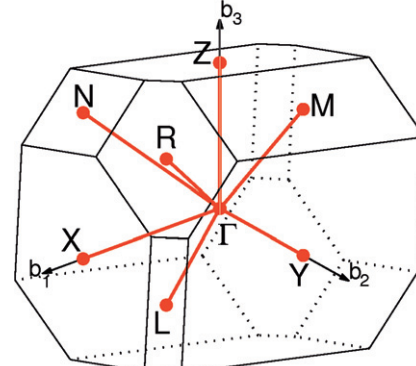


Fig. 22. Brillouin zone of TRI_{1a} lattice. Path: X- Γ -Y|L- Γ -Z|N- Γ -M|R- Γ . An example of band structure using this path is given in Fig. 47.

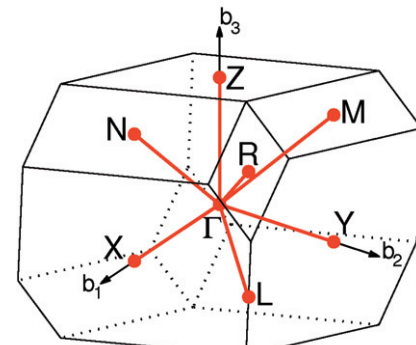


Fig. 23. Brillouin zone of TRI_{2a} lattice. Path: X- Γ -Y|L- Γ -Z|N- Γ -M|R- Γ .

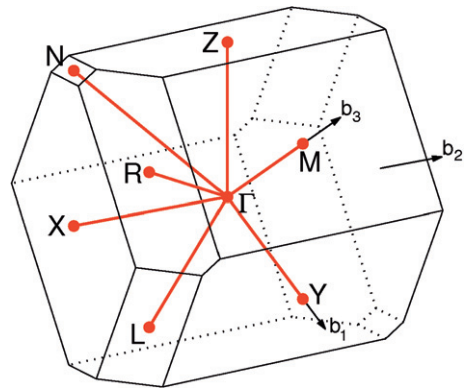


Fig. 24. Brillouin zone of TRI_{1b} lattice. Path: $X-\Gamma-Y|L-\Gamma-Z|N-\Gamma-M|R-\Gamma$. An example of band structure using this path is given in Fig. 48.

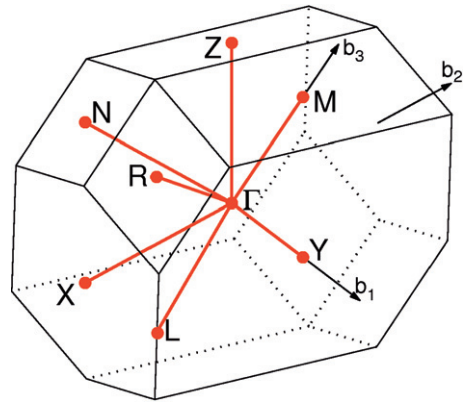


Fig. 25. Brillouin zone of TRI_{2b} lattice. Path: $X-\Gamma-Y|L-\Gamma-Z|N-\Gamma-M|R-\Gamma$.

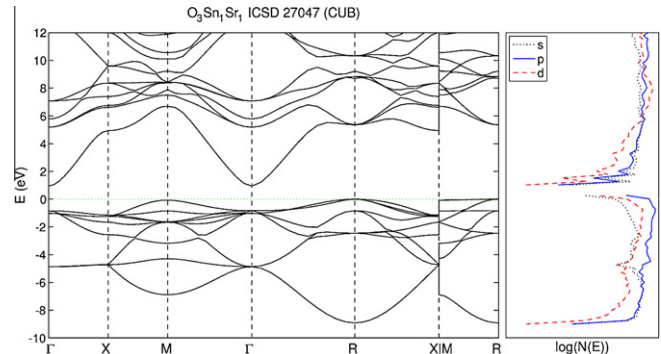


Fig. 26. Band structure of $\text{Sr}(\text{SnO}_3)$ in CUB lattice.

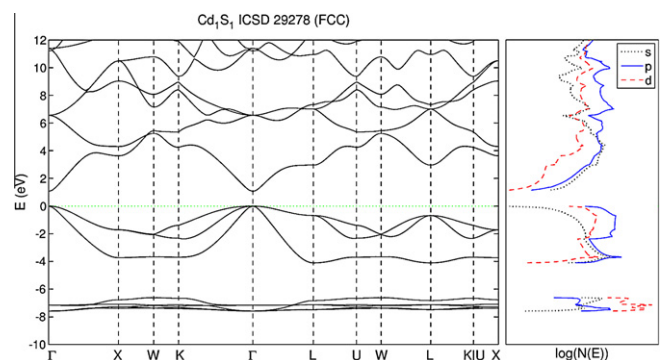


Fig. 27. Band structure of CdS in FCC lattice.

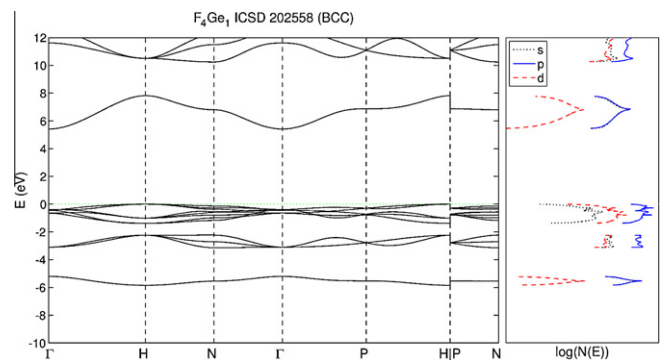


Fig. 28. Band structure of GeF_4 in BCC lattice.

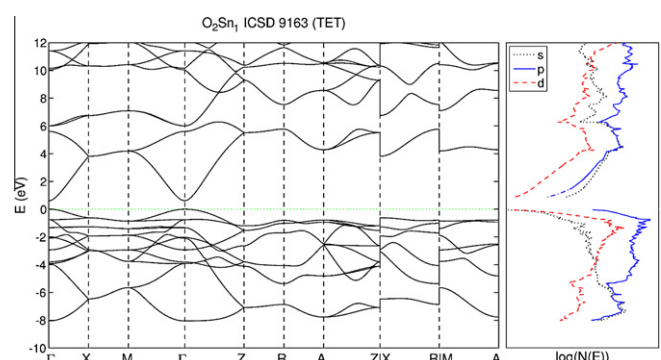


Fig. 29. Band structure of SnO_2 in TET lattice.

Table 20
Symmetry k-points of TRI_{1a} and TRI_{2a} .

$\times \mathbf{b}_1$	$\times \mathbf{b}_2$	$\times \mathbf{b}_3$	$\times \mathbf{b}_1$	$\times \mathbf{b}_2$	$\times \mathbf{b}_3$	
0	0	0	Γ	1/2	1/2	1/2 R
1/2	1/2	0	L	1/2	0	0 X
0	1/2	1/2	M	0	1/2	0 Y
1/2	0	1/2	N	0	0	1/2 Z

Table 21
Symmetry k-points of TRI_{1b} and TRI_{2b} .

$\times \mathbf{b}_1$	$\times \mathbf{b}_2$	$\times \mathbf{b}_3$	$\times \mathbf{b}_1$	$\times \mathbf{b}_2$	$\times \mathbf{b}_3$	
0	0	0	Γ	0	-1/2	1/2 R
1/2	-1/2	0	L	0	-1/2	0 X
0	0	1/2	M	1/2	0	0 Y
-1/2	-1/2	1/2	N	-1/2	0	1/2 Z

Variations:

TRI_{1a} : $k_\alpha > 90^\circ$, $k_\beta > 90^\circ$, $k_\gamma > 90^\circ$, $k_\gamma = \min \{k_\alpha, k_\beta, k_\gamma\}$

TRI_{1b} : $k_\alpha < 90^\circ$, $k_\beta < 90^\circ$, $k_\gamma < 90^\circ$, $k_\gamma = \max \{k_\alpha, k_\beta, k_\gamma\}$

TRI_{2a} : $k_\alpha > 90^\circ$, $k_\beta > 90^\circ$, $k_\gamma = 90^\circ$

TRI_{2b} : $k_\alpha < 90^\circ$, $k_\beta < 90^\circ$, $k_\gamma = 90^\circ$

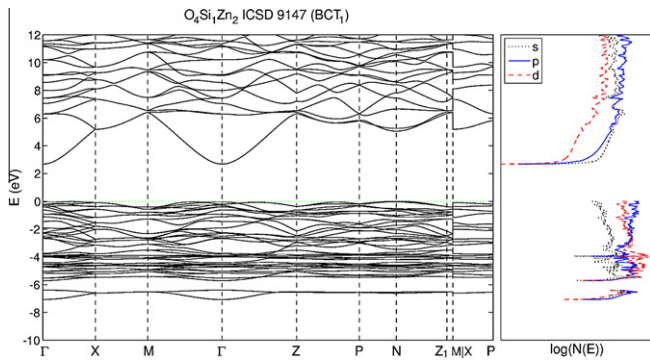
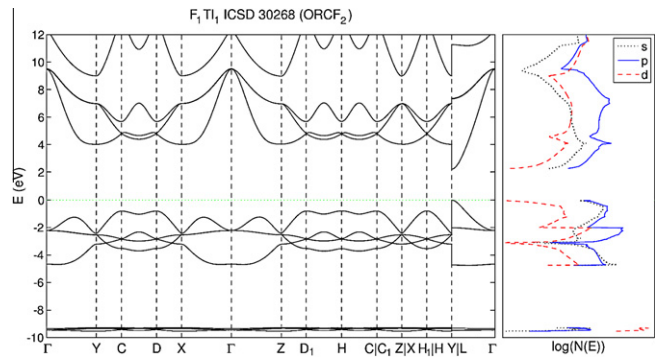
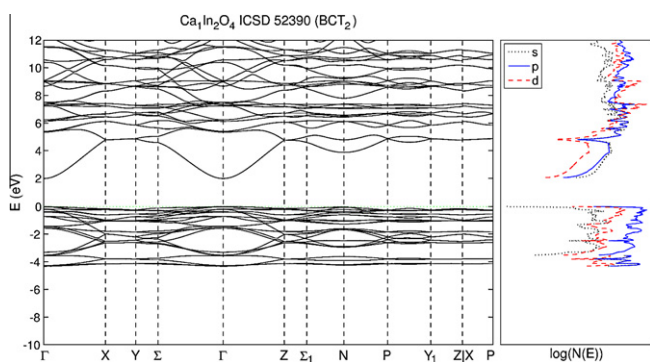
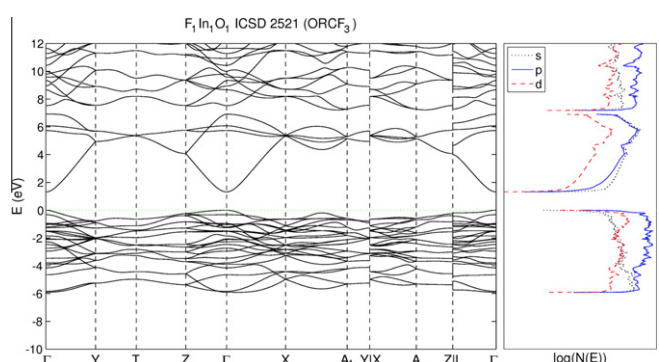
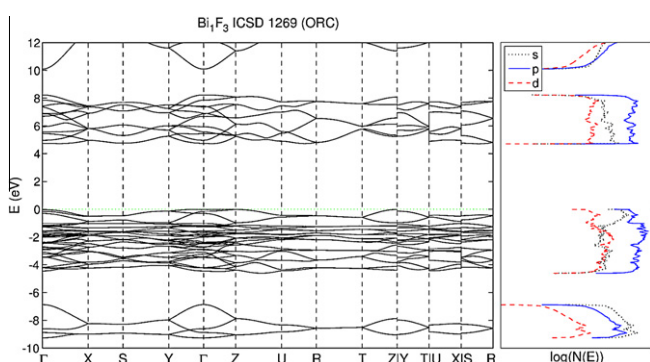
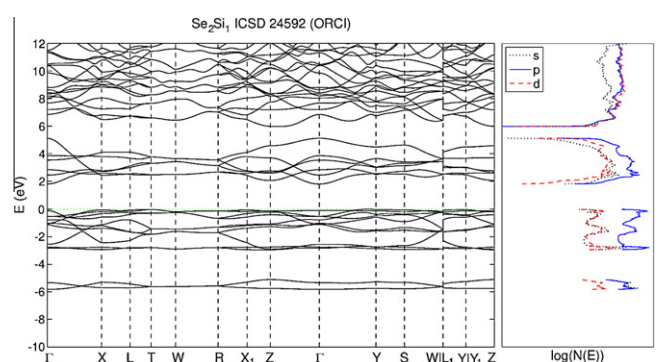
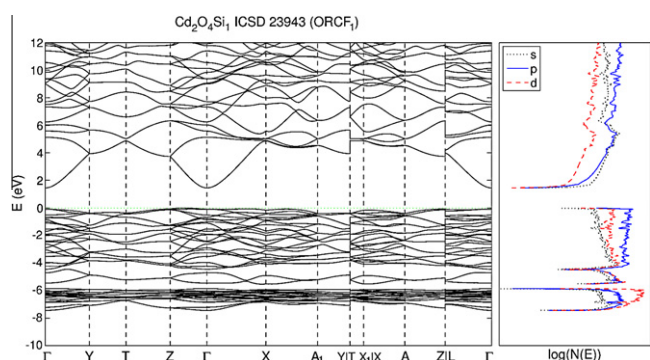
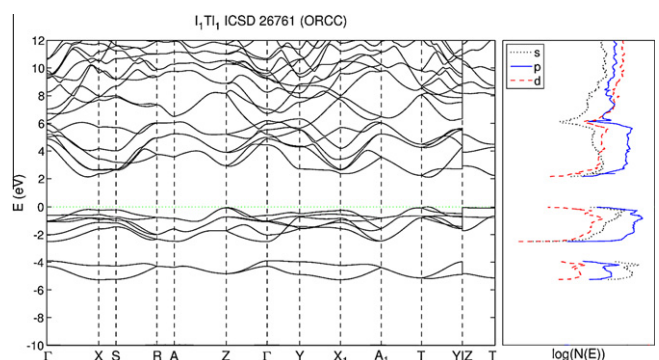
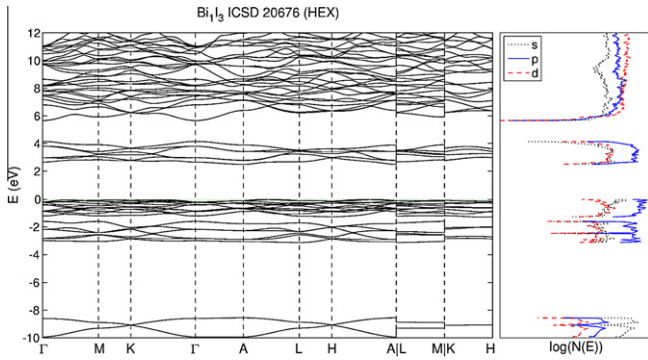
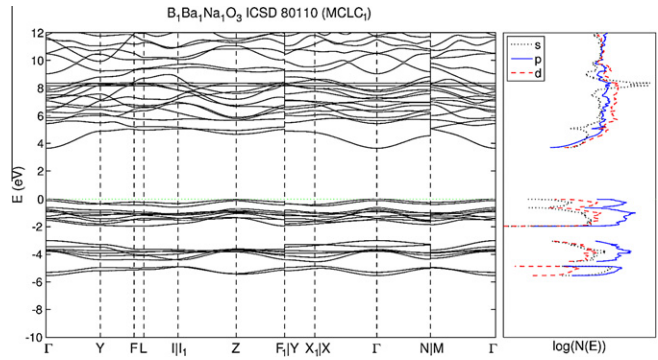
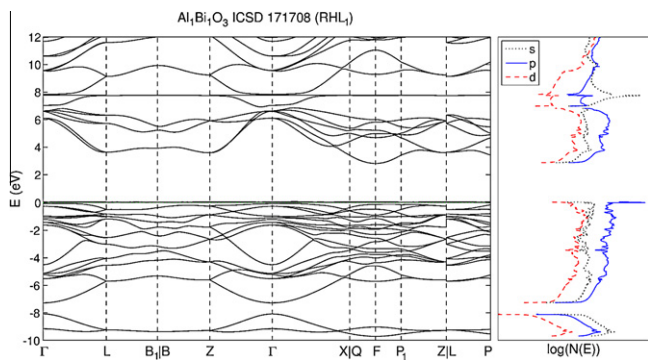
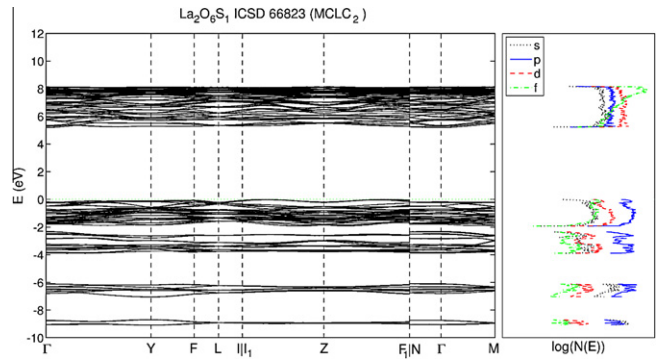
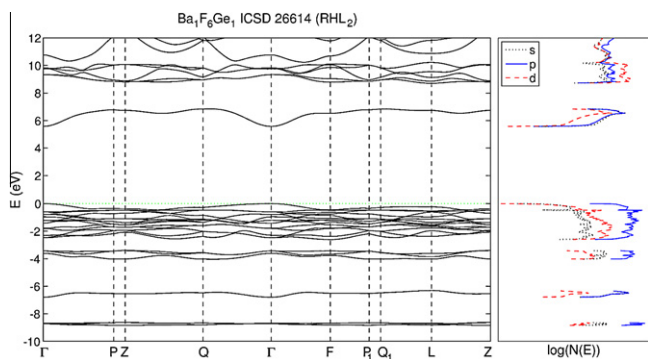
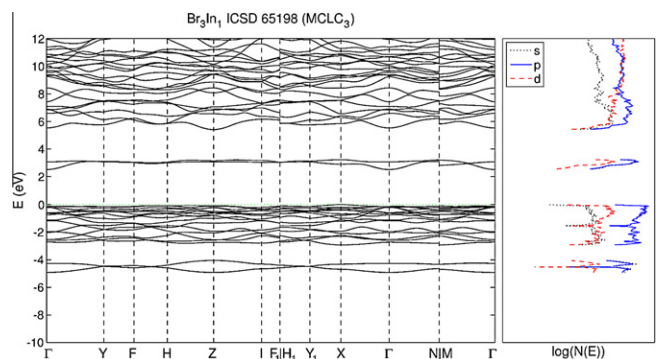
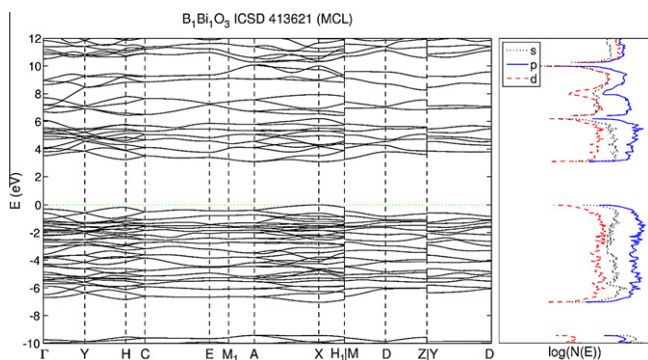
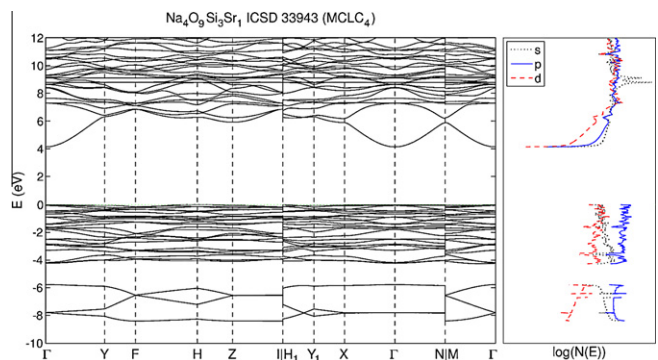
Fig. 30. Band structure of $\text{Zn}_2(\text{SiO}_4)$ in BCT₁ lattice.Fig. 34. Band structure of TiF in ORCF₂ lattice.Fig. 31. Band structure of CaIn_2O_4 in BCT₂ lattice.Fig. 35. Band structure of InOF in ORCF₃ lattice.Fig. 32. Band structure of BiF_3 in ORC lattice.Fig. 36. Band structure of SiSe_2 in ORCl lattice.Fig. 33. Band structure of $\text{Cd}_2(\text{SiO}_4)$ in ORCF₁ lattice.

Fig. 37. Band structure of TiI in ORCC lattice.

Fig. 38. Band structure of BiI_3 in HEX lattice.Fig. 42. Band structure of $\text{BaNa}(\text{BO}_3)$ in MCLC_1 lattice.Fig. 39. Band structure of BiAlO_3 in RHL_1 lattice.Fig. 43. Band structure of $(\text{LaO})_2(\text{SO}_4)$ in MCLC_2 lattice.Fig. 40. Band structure of $\text{Ba}(\text{GeF}_6)$ in RHL_2 lattice.Fig. 44. Band structure of InBr_3 in MCLC_3 lattice.Fig. 41. Band structure of $\text{Bi}(\text{BO}_3)$ in MCL lattice.Fig. 45. Band structure of $\text{Na}_4\text{Sr}(\text{SiO}_3)_3$ in MCLC_4 lattice.

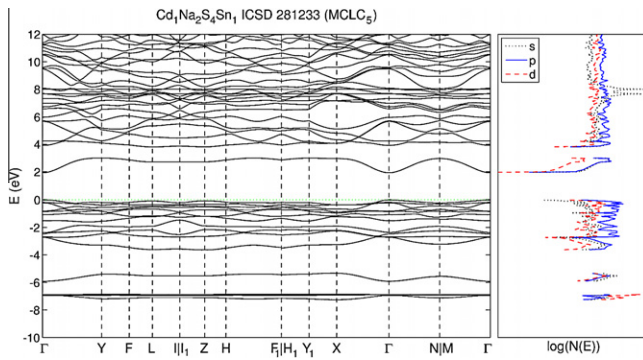


Fig. 46. Band structure of $\text{Na}_2(\text{CdSnS}_4)$ in MCLC_5 lattice.

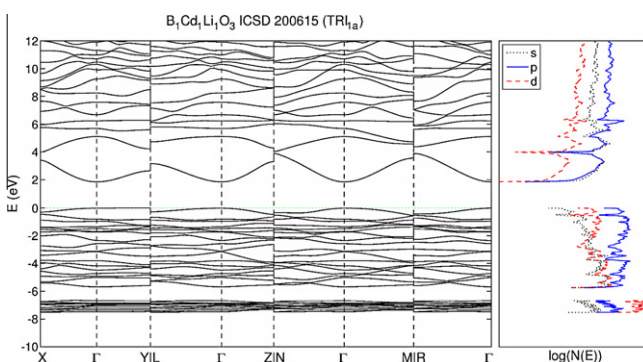


Fig. 47. Band structure of $\text{LiCd}(\text{BO}_3)$ in TRI_{1a} lattice.

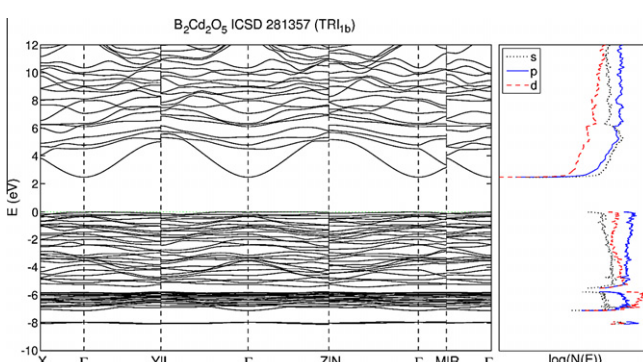


Fig. 48. Band structure of $\text{Cd}_2(\text{B}_2\text{O}_5)$ in TRI_{1b} lattice.

Appendix B

Selected examples of band structure for each shape of Brillouin zone are presented in this section. The Fermi energy is shifted to the valence band maximum at zero. In each figure, the orbital-projected total density of states $N(E)$ are plotted in the right panel in logarithmic scale (see Figs. 26–48).

References

- [1] X.D. Xiang, X. Sun, G. Brinceno, Y. Lou, K.-A. Wang, H. Chang, W.G. Wallace-Freedman, S.-W. Chen, P.G. Schultz, *Science* 268 (1995) 1738.
- [2] H. Koinuma, I. Takeuchi, *Nature Materials* 3 (2004) 429.
- [3] J.L. Spivack, J.N. Cawse, D.W. Whisenhunt, B.F. Johnson, K.V. Shalyaev, J. Male, E.J. Pressman, J.Y. Ofori, G.L. Soloveichik, B.P. Patel, T.L. Chuck, D.J. Smith, T.M. Jordan, M.R. Brennan, R.J. Kilmer, E.D. Williams, *Applied Catalysis A: General* 254 (2003) 5.
- [4] T.R. Boussie, G.M. Diamond, C. Goh, K.A. Hall, A.M. LaPointe, M. Leclerc, C. Lund, V. Murphy, J.A.W. Shoemaker, U. Tracht, H. Turner, J. Zhang, T. Uno, R.K. Rosen, J.C. Stevens, *Journal of the American Chemical Society* 125 (2003) 4306.
- [5] R.A. Potyrailo, B.J. Chisholm, W.G. Morris, J.N. Cawse, W.P. Flanagan, L. Hassib, C.A. Molaison, K. Ebziansky, G. Medford, H. Reitz, *Journal of Computational Chemistry* 5 (2003) 472.
- [6] R.A. Potyrailo, I. Takeuchi, *Measurement Science and Technology* 16 (2005) 1.
- [7] Y.-M. Chiang, D.R. Sadoway, M.K. Aydinol, Y.-I. Jang, B. Huang, G. Ceder, *Nature* 392 (1998) 694.
- [8] G.H. Jóhannesson, T. Bligaard, A.V. Ruban, H.L. Skriver, K.W. Jacobsen, J.K. Nørskov, *Physical Review Letters* 88 (2002) 255506.
- [9] D.P. Stucke, V.H. Crespi, *Nano Letters* 3 (2003) 1183.
- [10] S. Curtarolo, D. Morgan, K. Persson, J. Rodgers, G. Ceder, *Physical Review Letters* 91 (2003) 135503.
- [11] D. Morgan, G. Ceder, S. Curtarolo, *Measurement Science and Technology* 16 (2005) 296.
- [12] S. Curtarolo, D. Morgan, G. Ceder, *Calphad* 29 (2005) 163.
- [13] C.C. Fischer, K.J. Tibbetts, D. Morgan, G. Ceder, *Nature Materials* 5 (2006) 641.
- [14] T. Bligaard, G.H. Jóhannesson, A.V. Ruban, H.L. Skriver, K.W. Jacobsen, J.K. Nørskov, *Applied Physics Letters* 83 (2003) 4527.
- [15] M.P. Anderson, T. Bligaard, K.E.L.A. Kustov, J. Greeley, T. Jóhannesson, C.H. Christensen, J.K. Nørskov, *Journal of Catalysis* 239 (2006) 501.
- [16] O. Levy, R.V. Chepulskii, G.L.W. Hart, S. Curtarolo, *Journal of the American Chemical Society* 132 (2010) 833.
- [17] O. Levy, G.L.W. Hart, S. Curtarolo, *Journal of the American Chemical Society* 132 (2010) 4830.
- [18] A.N. Kolmogorov, S. Curtarolo, *Physical Review B* 73 (2006) 180501.
- [19] M. Calandra, A.N. Kolmogorov, S. Curtarolo, *Physical Review B* 75 (2007) 144506.
- [20] A.N. Kolmogorov, M. Calandra, S. Curtarolo, *Physical Review B* 78 (2008) 094520.
- [21] C. Wolverton, D.J. Siegel, A.R. Akbarzadeh, V. Ozolins, *Journal of Physics: Condensed Matter* 20 (2008) 064228.
- [22] D.J. Siegel, C. Wolverton, V. Ozolins, *Physical Review B* 76 (2007) 134102.
- [23] A.R. Akbarzadeh, V. Ozolins, C. Wolverton, *Advanced Materials* 19 (2007) 3233.
- [24] T.B. Massalski, H. Okamoto, P.R. Subramanian, L. Kacprzak (Eds.), *Binary alloy Phase Diagrams*, American Society for Metals, Materials Park, OH, 1990.
- [25] P. Villars, M. Berndt, K. Brandenburg, K. Cenzual, J. Daams, F. Hulliger, T. Massalski, H. Okamoto, K. Osaki, A. Prince, H. Putz, S. Iwata, *Journal of Alloys and Compounds* 367 (2004) 293.
- [26] A.D. Mighell, V.L. Karen, *Acta Crystallographica* A49 (1993) c409.
- [27] A. Belsky, M. Hellenbrandt, V.L. Karen, P. Luksch, *Acta Crystallographica* B58 (2002) 364.
- [28] J.K. Nørskov, T. Bligaard, J. Rossmeisl, C.H. Christensen, *Nature Chemistry* 1 (2009) 37.
- [29] G. Hautier, C. Fischer, A. Jain, T. Mueller, G. Ceder, *Finding nature's missing ternary oxide compounds using machine learning and density functional theory*, *Chemistry of Materials*, 2010.
- [30] C.J. Bradley, A.P. Cracknell, *The mathematical Theory of Symmetry in Solids: Representation Theory for Point Groups and Space Groups*, Clarendon Press, Oxford, 1972.
- [31] G. Burns, A.M. Glazer, *Space Groups for Solid State Scientists*, Academic Press, Boston, 1990.
- [32] S.C. Miller, W.F. Love, *Tables of Irreducible Representations of Space Groups and Co-Representations of Magnetic Groups*, Pruett Press, Boulder, 1967.
- [33] O.V. Kovalev, *Irreducible Representations of the Space Groups*, Gordon and Breach, New York, 1965.
- [34] A. Casher, M. Glucky, Y. Gur, *The Irreducible Representations of Space Groups*, W.A. Benjamin Inc., New York, 1969.
- [35] S. Curtarolo, G.L.W. Hart, W. Setyawan, M. Mehl, M. Jahnatek, R.V. Chepulskii, O. Levy, D. Morgan, *AFLOW: Software for High-Throughput Calculation of Material Properties*, 2009. <<http://materials.duke.edu/aflow.html>>.
- [36] P. Giannozzi, S. Baroni, N. Bonini, M. Calandra, R. Car, C. Cavazzoni, D. Ceresoli, G.L. Chiarotti, M. Cococcioni, I. Dabo, A. Dal Corso, S. de Gironcoli, S. Fabris, G. Fratesi, R. Gebauer, U. Gerstmann, C. Gougoussis, A. Kokalj, M. Lazzeri, L. Martin-Samos, N. Marzari, F. Mauri, R. Mazzarello, S. Paolini, A. Pasquarello, L. Paulatto, C. Sbraccia, S. Scandolo, G. Scaluzero, A.P. Seitsonen, A. Smogunov, P. Umari, R.M. Wentzcovitch, *Journal of Physics: Condensed Matter* 21 (2009) 395502.
- [37] P.Q. Nguyen, D. Stehlé, *ACM Transactions on Algorithms* 5 (2009) 1.
- [38] A.P. Cracknell, *Journal of Physics C: Solid State Physics* 6 (1973) 826.
- [39] W. Setyawan, R.M. Gaume, R.S. Feigelson, S. Curtarolo, *IEEE Transactions on Nuclear Science* 56 (2009) 2989.
- [40] V.L. Karen, M. Hellenbrandt, *Acta Crystallographica* A58 (2002) c367.
- [41] I.D. Brown, S.C. Abrahams, M. Berndt, J. Faber, V.L. Karen, W.D.S. Motherwell, P. Villars, J.D. Westbrook, B. McMahon, *Acta Crystallographica* A61 (2005) 575.
- [42] W. Kohn, L.J. Sham, *Physical Review* 140 (1965) A1133.
- [43] P.E. Blochl, *Physical Review B* 50 (1994) 17953; G. Kresse, J. Joubert, *Physical Review B* 59 (1999) 1758.
- [44] J.P. Perdew, K. Burke, M. Ernzerhof, *Physical Review Letters* 77 (1996) 3865.
- [45] H.J. Monkhorst, J.D. Pack, *Physical Review B* 13 (1976) 5188.
- [46] W. Setyawan, R.D. Diehl, S. Curtarolo, *Physical Review Letters* 102 (2009) 055501.
- [47] R.D. Diehl, W. Setyawan, S. Curtarolo, *Journal of Physics: Condensed Matter* 20 (2008) 314007.
- [48] F. Aryasetiawan, O. Gunnarsson, *Reports on Progress in Physics* 61 (1998) 237.

- [49] S.L. Duradev, G.A. Botton, S.Y. Savrasov, C.J. Humphreys, A.P. Sutton, Physical Review B 57 (1998) 1505.
- [50] A.I. Liechtenstein, V.I. Anisimov, J. Zaanen, Physical Review B 52 (1995) R5467.
- [51] V. Leiria Campo Jr., M. Cococcioni, Journal of Physics: Condensed Matter 22 (2010) 055602.
- [52] J.K. Lang, Y. Baer, P.A. Cox, Journal of Physics F: Metal Physics 11 (1981) 121.
- [53] D. Wegner, A. Bauer, Y.M. Koroteev, G. Bihlmayer, E.V. Chulkov, P.M. Echenique, G. Kaindl, Physical Review B 73 (2006) 115403.
- [54] Y. Jiang, J.B. Adams, M. van Schilfgaarde, Journal of Chemical Physics 123 (2005) 064701.
- [55] B.N. Harmon, V.P. Antropov, A.I. Liechtenstein, I.V. Solovyev, V.I. Anisimov, Journal of Physics and Chemistry of Solids 56 (1995) 1521.
- [56] H. Harima, Journal of Magnetism and Magnetic Materials 226 (2010) 83.
- [57] V.N. Antonov, B.N. Harmon, A.N. Yaresko, Physical Review B 63 (2001) 205112.
- [58] T. Jeong, Journal of Physics: Condensed Matter 18 (2006) 6769.